Plasma Sources Science and Technology

Time-resolved optical emission spectroscopy in CO_2 nanosecond pulsed discharges

To cite this article before publication: Matteo Ceppelli *et al* 2021 *Plasma Sources Sci. Technol.* in press https://doi.org/10.1088/1361-6595/ac2411

Time-Resolved Optical Emission Spectroscopy in CO_2 Nanosecond Pulsed Discharges

M. Ceppelli[1]‡, , T.P.W. Salden[1,2]‡, L. M. Martini[1], G. Dilecce[3,1]§ and P. Tosi[1,3]

[1]Dipartimento di Fisica Università di Trento, Via Sommarive 14, 38123 Povo - Trento, Italy

[2]Department of Applied Physics, Eindhoven University of Technology, 5600 MB Eindhoven, The Netherlands

[3]CNR Institute for Plasma Science and Technology, via Amendola 122/D, 70126 Bari, Italy

Abstract.

Nanosecond repetitively pulsed discharges at atmospheric pressure have shown comparatively high performances for CO_2 reduction to CO and O_2. However, mechanisms of CO_2 dissociation in these transient discharges are still a matter of discussion. In the present work, we have used time-resolved optical emission spectroscopy to investigate the CO_2 discharge progression from the initial breakdown event to the final post-discharge. We discover a complex temporal structure of the spectrally resolved light, which gives some insights into the underlying electron and chemical kinetics. We could estimate the electron density using the Stark broadening of O and C lines and the electron temperature with C^+ and C^{++} lines. By adding a small amount of nitrogen, we could also monitor the time evolution of the gas temperature using the Second Positive System bands of N_2. We conclude that the discharge evolves from a breakdown to a spark phase, the latter being characterised by a peak electron density around $10^{18}\,cm^{-3}$ and a mean electron temperature around 2 eV. The spark phase offers beneficial conditions for vibrationally enhanced dissociation, which might explain the high CO_2 conversion observed in these plasma discharges.

Keywords: plasma diagnostics, spectral line broadening, optical emission spectroscopy, nanosecond repetitively pulsed plasma, CO_2 discharge.

Submitted to: *Plasma Sources Sci. Technol.*

‡ M. Ceppelli and T.P.W. Salden have equally contributed to the paper

§ corresponding author

1. Introduction

Nanosecond Repetitively Pulsed (NRP) discharges have shown good performances in the reduction of CO_2, both in dry reforming [1, 2] and in pure CO_2 [3–5]. The fast transient nature of NRP discharges calls for time-resolved diagnostics for understanding mechanisms and the time evolution of the discharge. In [3], Collisional Energy-Transfer Laser-Induced Fluorescence, CET-LIF [6, 7], was used to measure the development of the CO_2 dissociation after the discharge pulse. These results were later updated in [8] with new, non-thermal collision rate constants for the CET-LIF analysis. It was found that the dissociation at the end of the discharge pulse achieves extremely high values, around 70 %, followed by a decrease down to about 20 % after 150 µs, in agreement with the final dissociation value found in the effluent gas. Such a reduction is likely ascribable to both recombination kinetics and recirculation of untreated gas. Improvement of the conversion performances was pursued in [5] by changing the temporal pattern of the repeated pulses. Instead of continuous repetition of equally spaced pulses, excitation was grouped into repetitive bursts, each made of few pulses separated by a short time interval down to about 10 µs. The rationale for such a choice was to build up hot vibrational distributions to promote a vibrational dissociation channel. The eventual side effect of promoting thicker discharge channels is to enclose a larger fraction of the inlet gas column. The analysis of effluent products returned an improvement of dissociation performances with the burst pattern compared with the continuous one, both in dissociation degree and energy efficiency. One of the reasons can be looked for in the discharge characteristics. As shown in [5], a complex structure of the temporal development of voltage, current and global light emission (not spectrally resolved) is observed. In the continuous mode and the first pulse of a burst, the discharge pulse is made of three temporal regions, extending even beyond 1 µs after the beginning. The first region, in which the breakdown occurs, is characterised by the high voltage required for the discharge ignition, a relatively low charge density, and the duration of 10-20 ns. Most of the pulse energy is dissipated in this part of the pulse. The second and third regions are due to the reflected power travelling back and forth along the 3 m long output cable and a self-re-triggering after about 400 ns. Since the gas is still residually ionised by the first event and less dense, a low voltage is sufficient to ignite multiple discharge events. In a burst, with sufficiently short time separation between the pulses, the second and further pulses have characteristics similar to those of the

second and third regions of the first pulse. Two very different discharge regimes were then manifested in our previous research: the initial phase of the first pulse, characterised by relatively high electron energy and low charge density, and a regime with relatively low electron energy and higher charge density. The prevalence of the second regime in the burst mode might be at the origin of its improved dissociation performance. Such a picture was supported by voltage-current measurements only. This paper aims to deepen the time-resolved characterisation of the pulsed discharge regimes by analysing the emission spectra of the NRP discharge used in [5].

Time-resolved emission spectroscopy studies of NRP discharges in CO_2 are not yet available in the literature. Studies in nitrogen and air mixture have been reported, mainly devoted to a characterisation of the spark regime and the streamer-to-spark transition [9–11]. The Second Positive System (SPS) molecular nitrogen bands are readily observed in the streamer phase, neutral and ionised atomic lines prevail in the spark regime. In these papers, the rotational analysis of SPS bands was used to estimate the gas temperature in the streamer phase. In the spark regime, the excitation temperature of N^+ lines was taken as a measurement of the electron and gas temperature under the hypothesis of complete equilibrium between the electron and ion/neutral gas due to the high values of charge density. The latter was measured from the Stark broadening of N^+ lines. The resulting picture is a regime, called *thermal spark* in [11], with charge densities as high as about $1.5 \cdot 10^{19}\,\mathrm{cm}^{-3}$, almost full ionization, and a maximum (electron and gas) temperature close to 50 000 K. Similar observations were reported in [12, 13] for surface discharges in air. Continuous microwave (MW) discharges in CO_2 were investigated by emission spectroscopy in [14–16]. The dominant emissions were identified as the CO Third Positive and Angstrom systems, O I lines, and a continuum attributed to the $\mathrm{CO}(X) + \mathrm{O}(^3P) \rightarrow \mathrm{CO_2}(X) + h\nu$ chemiluminescent recombination reaction. By adding 5 % of N_2 to the gas, the SPS emission could be used to determine the gas temperature. In [15], nitrogen was used as an actinometer to infer the CO density from the CO Angstrom system and SPS system intensities ratio, to trace the CO_2 dissociation. In [17], in a RF plasma torch at low pressure (1–2 mbar), the CO+O continuum was used to monitor the CO_2 dissociation. Finally, in a MW discharge, the possibility of using the C_2 Swan bands for the measurement of the gas temperature was examined in [18].

In this paper, we analyse the time-resolved spectra in the diverse regimes, assign the spectral features and discuss their utilisation as a diagnostic tool, including the

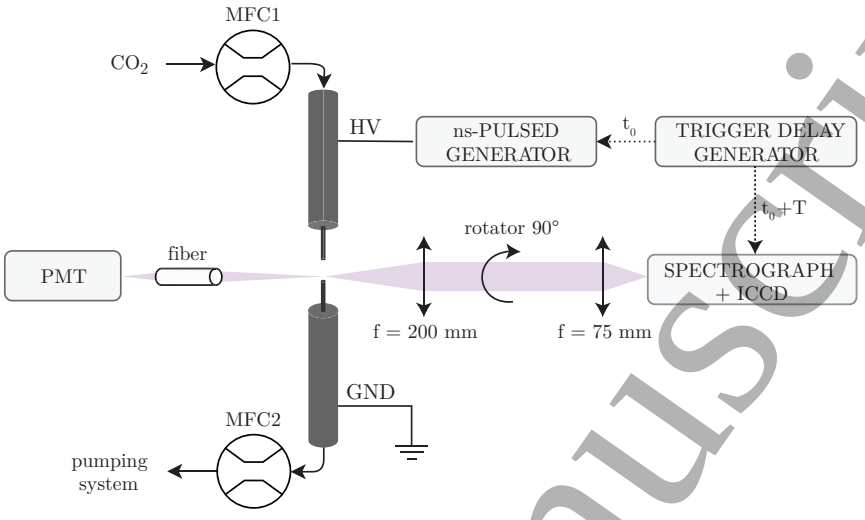

Figure 1. Schematic drawing of the experimental apparatus. MFC: Mass-Flow Controller; ICCD: Intensified CCD; PMT: Photomultiplier.

spectra obtained by the addition of a small N_2 amount. In particular we utilise the Stark broadening of the O I line at 777 nm for electron density estimates and the N_2 SPS emission as a spectroscopic thermometric tool. Finally, we draw some conclusion on the discharge characteristics in the continuous and burst modes.

2. Experimental Apparatus

The scheme of the experimental apparatus is shown in figure 1. The plasma conversion of CO_2 was carried out in a stainless steel vacuum-tight reactor with the electrodes arranged in a pin-to-pin configuration. The HV and ground electrodes were narrow stainless steel tubes that also served as inlet and outlet for the gas flow respectively. The HV electrode (int. diameter 1.07 mm, ext. diameter 1.47 mm) was kept above the grounded electrode (int. diameter 2 mm, ext. diameter 3.2 mm) at a fixed inter-electrode distance of 5 mm.

The discharge was ignited by a ns-pulsed power supply (NPG18/100k, Megaimpulse Ltd.), triggered by a waveform generator (Rigol DG4062). The ns-pulsed power supply features high voltage pulses with FWHM of 10 ns and rise time < 4 ns on a 75 Ω matched load, up to a frequency of 100 kHz and a maximum of 4000

pulses per second. The output voltage is selected by a knob that allows spanning from 50 % to 100 % of the maximum voltage (and pulse energy). Variation of the power supply output is then referenced as a percentage value of the maximum. The voltage at the load is measured case by case. Two different pulsing schemes were adopted for the measurements, as in [5]: (a) equally spaced pulses at a frequency of 200 Hz or 1 kHz (continuous mode); (b) sets of a fixed number of high-frequency pulses up to 100 kHz, with the sets being repeated at 200 Hz (burst mode). The applied voltage $V(t)$ and the current $i(t)$ flowing in the discharge were measured by a high voltage probe (P6015A, Tektronix) and an I/V converter (CT-D-1.0, Magnelab), respectively. A digital oscilloscope (Teledyne LeCroy HD9100) was used to record the signals.

The discharge was run at atmospheric pressure. A variable flow of CO_2 was injected into the reactor by an MKS mass flow controller (MFC1). A proportional-integral-derivative (PID) control acting on a second mass flow controller (MFC2) at the exit of the reactor, stabilised the pressure at 745 Torr. Pressure was monitored by a capacitive gauge (Varian Ceramicel FS 1000 Torr) providing input for the PID and evacuation/circulation of the gas were guaranteed by an Edwards 80 $m^3\,h^{-1}$ two-stage rotary vane pump and a mechanical booster.

The light emitted by the discharge was simultaneously detected by two sensors:

(i) a PMT (Hamamatsu R2949) coupled with a collection optical fiber, which returned the time-resolved emission profile. A set of neutral metallic filters (Thorlabs NDUV series) was used to prevent saturation of the PMT;

(ii) a spectrograph, composed of a 300 mm focal length monochromator (Shamrock SR303i-b), and an intensified gateable CCD (Andor iStar DH334T-18U-03, 1024x1024 pixels). The emitted light was collected by a 200 mm focal length lens placed at a distance f from the reactor vertical axis. The spectrograph was calibrated for relative irradiance by an Avantes Avalight-DH-BAL-CAL. The inter-electrode axis was imaged orthogonal to the input slit of the spectrograph by a periscope. The image was focused at the entrance slit of the spectrograph by a 75 mm focal length lens. The 50 µm input slit captures about 130 µm of the discharge gap in the centre of the gap. Three dispersion gratings (2400 gr mm^{-1}, 1200 gr mm^{-1}, 600 gr mm^{-1}) were alternatively used to get different spectral resolutions and spectral windows. The camera could be gated down to a minimum gate width of 2 ns. An external trigger signal allowed to synchronise the gate to the discharge with an adjustable delay (T). When needed, two longpass filters (Thorlabs FEL 0400, FEL 0550) were

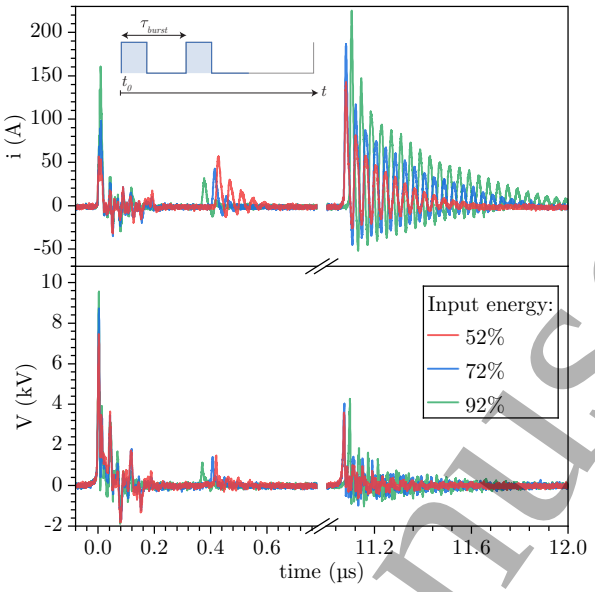

Figure 2. Voltage and current characteristics at three input voltage/energy, indicated as a fraction of the maximum output.

interposed between the reactor and the spectrograph to suppress the higher orders of the diffraction grating.

3. Macroscopic discharge characterisation

There are two kinds of discharge pulses: the first pulse of a burst, $N = 1$, and the successive $N \geq 2$ pulses. The first pulse always has the same characteristics as the continuous mode pulses. We shall refer to it as *Type I* pulse. The successive pulses are different from *Type I*, but similar to each other for any $N \geq 2$. We shall call them *Type II* pulses. We have analysed only burst sequences made of two pulses. This paper will report on three discharge conditions obtained by setting the power supply at 52 %, 72 % and 92 % of the maximum output voltage/energy. The voltage and current of both pulse types are shown in figure 2. Figure 3 and figure 4 report the voltage, the spectrally unresolved emission and the energy of *Type I* and *Type II* pulses, respectively. Four temporal regions can be recognised. The first one is the breakdown discharge, characterised by the high voltage required for initiating the discharge. In the second and third regions a low voltage is sufficient to ignite

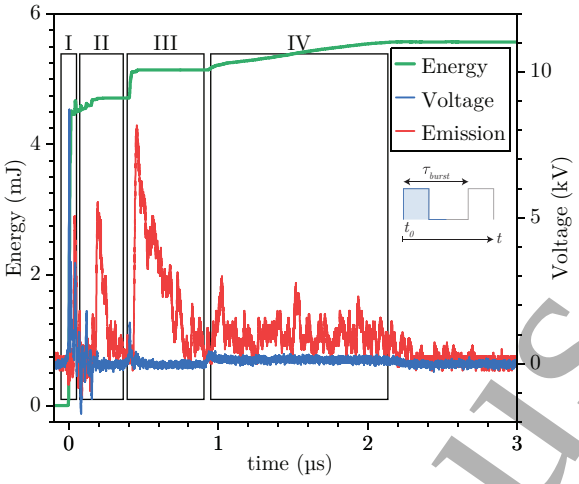

Figure 3. *Type I* pulse: time-resolved voltage, dissipated energy profiles, and spectrally unresolved emission profile gathered by a photomultiplier tube (PMT). Annotated regions correspond to the breakdown (I), reflected power (II), retriggering (III) and smooth voltage/current decay (IV) phases of the discharge. The emission is plotted with an arbitrary vertical scale to fit into the plot.

multiple discharges since the first event already ionised the gas. The spectrally unresolved light, captured by a photomultiplier, also evolves, with a long-lasting emission gradually appearing and superimposing to the one produced by the current alone. The fourth region is similarly due to a further slight voltage increase and current. On increasing the power supply voltage, the onset of Regions II, III and IV moves towards earlier times.

In *Type II* pulses, the voltage and current show a more regular behavior, with a single region in which the whole pulse energy is consumed in a sequence of short-period voltage and current oscillations. *Type I* pulses are always observed in the continuous mode and when the interval between pulses is roughly larger than 100 µs [5]. We may state that *Type II* pulses appear whenever the second (and successive) pulse is fired in a discharge gap that preserves a memory of the previous pulse, which is a combination of changed gas composition, lower overall density, and higher temperature; in other words, when the pulse encounters a different load impedance that changes the way electric power is deposited into the plasma.

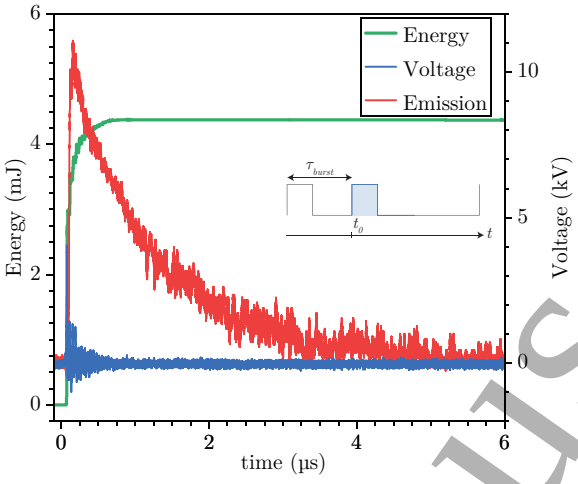

Figure 4. Time-resolved voltage and dissipated energy profiles of a *Type II* pulse along with spectrally unresolved emission profile gathered by a photomultiplier tube (PMT). The emission is plotted with an arbitrary vertical scale to fit into the plot.

4. Results and discussion

Spectra recorded at three delays after the discharge ignition are reported in figure 5, for *Type I* pulses. The three delays are representative of: Region I (0 ns, figure 5 (a)), the start of Region III (400 ns, figure 5 (b)) and the late Region IV (2000 ns, figure 5 (c)). Spectra of Region II are similar to those of Region III. The observed drastic changes between the spectra must be ascribed to changes in the plasma and the appearance of new neutral and ionised species. In addition to recognisable CO_2^+, CO and C_2 emissions, we observe continuum and unknown bands appearing along the time evolution of the discharge pulses. In sections 4.4 and 4.5 a detailed discussion of the time-resolved spectra in *Type I* and *Type II* pulses, respectively, will be provided. For a better understanding of the spectral features we shall start by addressing the measurement of electron density (section 4.1), electron temperature (section 4.2), and gas temperature (section 4.3). To this end, we focus now on the presence and time evolution of atomic lines.

Intense atomic lines (C, C^+, C^{++} and O) are present in the spectra. Their temporal evolution is reported in figure 6. Ionic carbon lines appear in Regions II and III in correspondence with the discharge current peaks. It is then reasonable

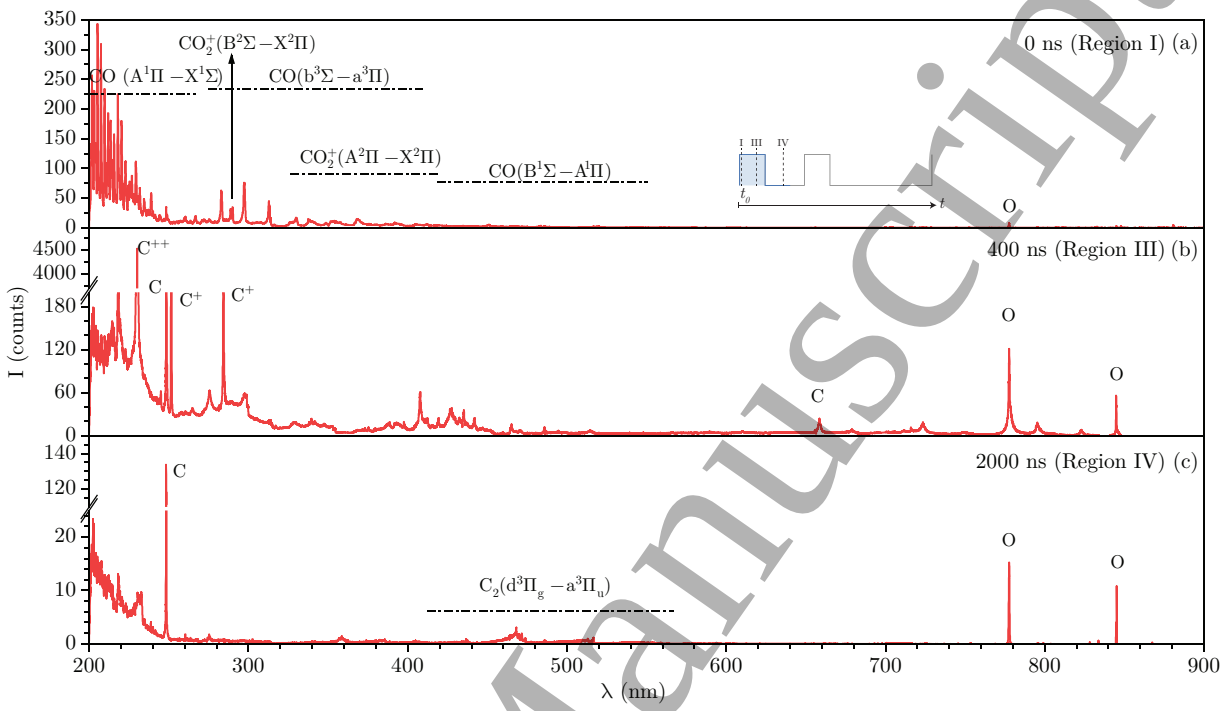

Figure 5. Emission spectra of *Type I* pulses at three delays after the pulse start. Discharge operating at 1 kHz (CW) in pure CO_2 feed gas.

to ascribe these lines to electron impact excitation and, as we shall discuss later in section 4.2, to a partial local thermodynamic equilibrium (LTE) between electrons and electronic excitation and ionisation. Neutral atomic C and O lines have a different time evolution instead since they persist well beyond the current and the ionic lines. We then attribute these lines to energy-transfer processes involving long-living species and/or recombination processes. The O line in Region I is an exception to this as its behavior is similar to the current, suggesting again an origin from electron impact. At present, we have not yet identified the precursors of these lines. In Region II and III, the O(777 nm) line starts to be visible before all the C lines. This is understandable considering that O is the product of a one-stage dissociation of CO_2, namely the electron impact $e + CO_2 \rightarrow CO + O + e$. C lines need a further dissociation stage of CO. The O(777 nm) and C(247 nm) lines, although their origin is not well understood, will be very useful for the estimation of the electron density by Stark line broadening (see section 4.1). Ionic lines, instead, allow estimating the

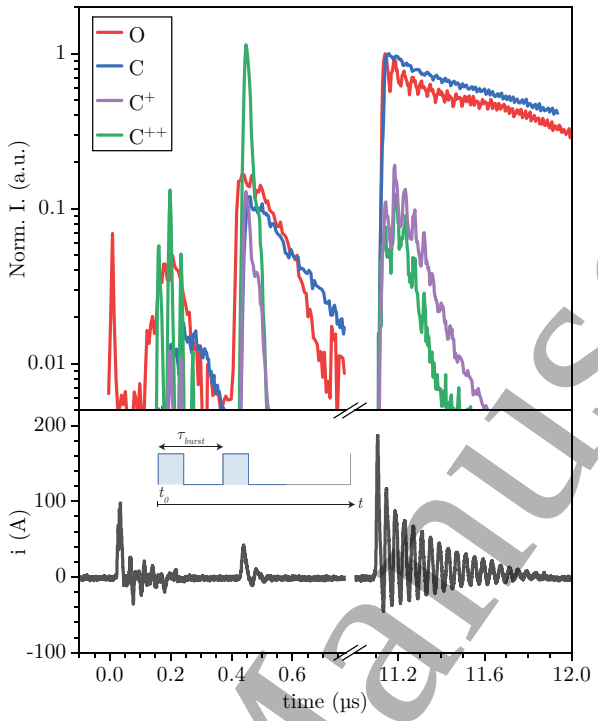

Figure 6. Temporal evolution of atomic lines along the first (*Type I*) and second (*Type II*) pulses of a 2-pulse burst, at 72 % of power supply output. Lines: C at 247.85 nm; C^+ at 250.912 nm and 251.206 nm; C^{++} at 229.68 nm; O at 777.194, 777.417, 777.539 nm (triplet). The current is reported in the bottom plot as a timing reference.

electron temperature (section 4.2).

4.1. Electron density from Stark broadening

To infer the electron density (n_e) from spectral line Stark broadening we use the oxygen $3s\ ^5S_0 \leftarrow 3p\ ^5P^{J=1,2,3}$ lines – a triplet at 777.194 nm, 777.417 nm and 777.539 nm – and the carbon $2p\ ^1S \leftarrow 3s\ ^1P$ line at 247.85 nm. Details of the measurement and analysis of the line broadening are given in Appendix A. Figure 7 shows the calculated n_e for the discharge running at 200 Hz in 90.0 kHz burst mode, for different input energies.

The electron density values reported in the plots are only those we consider

reliable because the O line signal is well measurable and an additional broadening is safely distinguishable from the instrumental function. In Region I of the first pulse, although the O line is readily observable, no reliable further broadening is measurable. With the current experimental setup, the lower detection limit for n_e is $10^{17}\,\mathrm{cm}^{-3}$. The observed behavior of n_e is in line with current/voltage measurements. In Region I, a low electron density is expected. In Region II and III, despite a low discharge voltage, n_e raises to values around $10^{18}\,\mathrm{cm}^{-3}$, justifying the classification of these discharge regions as a spark regime. The spark regime starts at progressively smaller delays on increasing the power supply energy setting, up to a condition in which, at 92 %, Region II is no more separated from Region I. Increasing the input energy results in a higher electron density in Region II of the first pulse. On the contrary, in both Region III and the second pulse, n_e decreases, albeit current and deposited energy regularly increase (see figure 3). This might be due to the increasing size of the discharge channel cross-section.

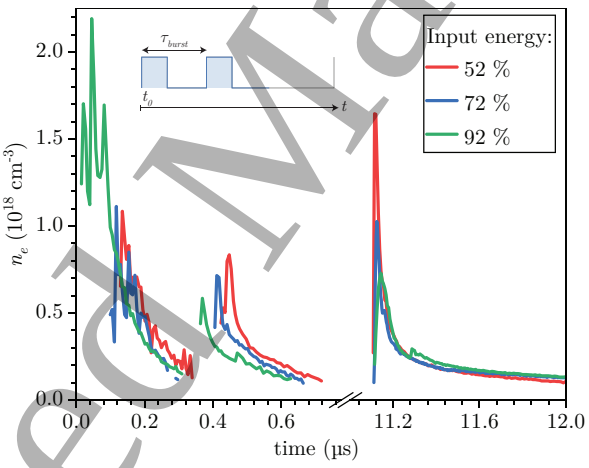

Figure 7. Temporal electron density profiles from Stark broadening for different input energy setting. Discharge at 200 Hz in two pulse 90.0 kHz burst mode, with 300 sccm CO_2 gas flow at 745 Torr. Densities are calculated for T_e of 20 000 K and assuming T_g to decay as a single exponential per pulse based on data from figure 10. The electron density n_e is the average of calculations with TOPbase and NIST-LSJ broadening parameters A1. Discharge starting at 0 ns.

4.2. Electron temperature estimate

The availability of carbon ion lines, together with the large electron density, makes it possible to estimate the electron temperature based on the hypothesis of an LTE condition in the spark regime. According to the McWhirter criterion [19], in a carbon plasma LTE is achieved for $n_e \gtrsim 10^{17}\,\mathrm{cm}^{-3}$ [20]. The fulfillment of LTE allows using the Boltzmann distribution function and the Saha ionisation equilibrium for the calculation of the population of electronic levels and the simulation of emission spectra. To this end, full LTE is not strictly required, but rather what is called in [21] 'an electron excitation kinetics (EEK) condition', in which the excitation temperature of atomic levels is equal to the electron temperature, $T_{exc} = T_e$. Eligible atomic lines for the measurement of T_{exc} must be those excited by electron impact only. From the discussion on the data of figure 6, the ionic C lines fulfill this requirement, while we must rule out from this analysis the neutral C line since it is the result of energy transfer processes with long-living species. We have fitted the spectra including the C^{++} and C^{+} lines by the NIST-LIBS online simulation tool [22], using the measured n_e values and evaluating an error bar due to the 60 % uncertainty in the measured electron density. Two such fitted spectra are shown in figure 8, and measured values of T_e are plotted in figure 9 together with n_e curves, for the 92 % power supply energy. The other energy cases show similar results.

The electron temperature basically evolves according to the discharge voltage, decreasing in regions II and III qualitatively in the same way as the amplitude of the voltage ringings. Unfortunately a measurement in region I was not possible. We can instead state that in most of the spark discharge phase, the electron temperature maintains a value roughly between 2 and 2.5 eV.

It is worth pointing out here that these electron temperature values have to be taken as estimates only. The LIBS calculations are done in an ideally pure carbon plasma, while we are in a complicated gas mixture including molecular components at high pressure. At these large ionisation degrees, however, the electron kinetics should still be dominant. The rate constants of energy exchanges between atomic levels by electron collision are in fact of the order of $10^{-4} - 10^{-5}\,\mathrm{cm}^3\mathrm{s}^{-1}$, to be compared with those of processes induced by molecular collisions, not exceeding $10^{-9}\,\mathrm{cm}^3\mathrm{s}^{-1}$.

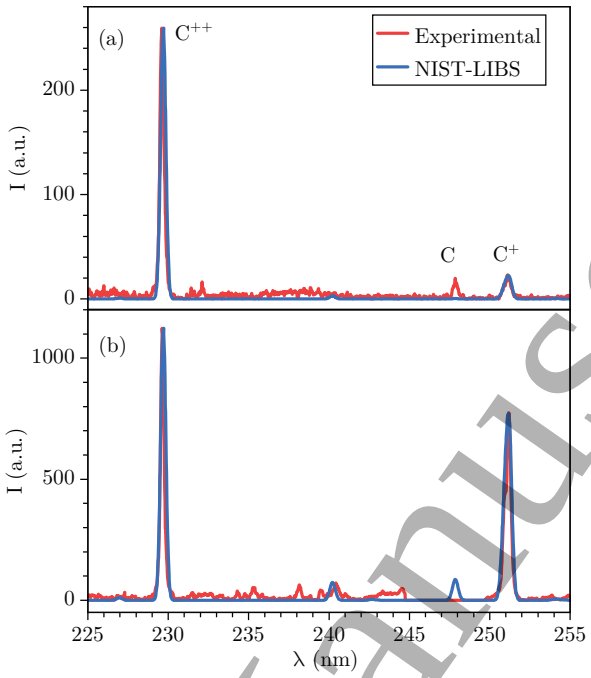

Figure 8. Experimentally obtained C^+ and C^{++} spectra during first (a) and second pulse (b) compared with simulated pure C LIBS spectra from [22], which assume Saha-LTE. Spectra recorded 140 ns after voltage pulse onset. Discharge operated at 200 Hz in 90.0 kHz burst mode in 300 sccm CO_2 at 745 Torr and 92 % input energy. C(247 nm) line removed from the spectrum (b) for ease of overlapping simulation with recorded data.

4.3. Spectroscopic gas temperature

We have measured the time dependent gas temperature by analysing the rotational temperature of the $N_2(C^3\Pi_u - B^3\Pi_g)$ Second Positive System (SPS) emission, made possible by the injection of 5 % of N_2 to the gas feed flux. The validity of this approach, together with a broader discussion on spectroscopic thermometry, is deferred to Appendix B. We have chosen the (0,0) band at 337 nm since it is the strongest and least overlapped with other emissions. In the first pulse of a burst these emissions are strong in Region I up to about 15 ns, reappear weakly in the first few ns of Region II and Region III, and at the beginning of a *Type II* pulse. In the particular case of the second pulse, because few ns are a too short time for heating the gas, the observed temperature reproduces the gas temperature immediately before the onset

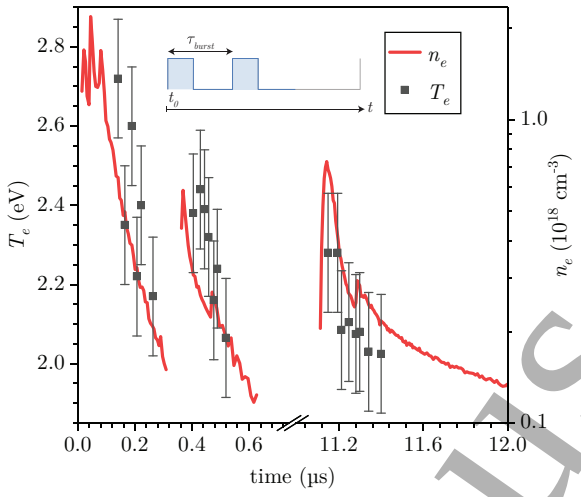

Figure 9. Estimated T_e from LIBS spectra simulation such as in figure 8 along with calculated n_e from figure 7. Confidence intervals are calculated from uncertainty in electron density. Same discharge conditions as in figure 8.

of the pulse. By changing the time lag between the pulses in the burst, we can observe the temperature decay after the first pulse. The minimum achievable inter-pulse time is 10 µs due to the power supply limitations. Temperature measurements are shown in figure 10. A double exponential function can reasonably well reproduce the T_{rot} decay after the pulse. With a time constant of about 17 µs, the fast component is likely due to a rapid expansion after the strong temperature rise in the discharge. With characteristic time close to 500 µs, the slow one is likely due to ongoing mixing with the surrounding cold gas. Backward extrapolation in the 2-10 µs interval, where the discharge current is zero, results in a reasonable estimation of the maximum temperature reached in the discharge of around 2400 K. The physical soundness of this double exponential behaviour cannot be discussed here without complete modeling including the fluid-dynamics after the spark. It is nevertheless clear that the gas cooling proceeds along two phases.

The temperature measurements by LIF excitation spectra reported in [3] are also shown in figure 10. Apart from small differences in the discharge conditions, LIF temperatures are always considerably larger than the SPS ones. This issue deserves a discussion. LIF thermometry is based on tuning the laser to two or more ro-vibronic transitions starting from different rotational levels. In [3] we basically used two close

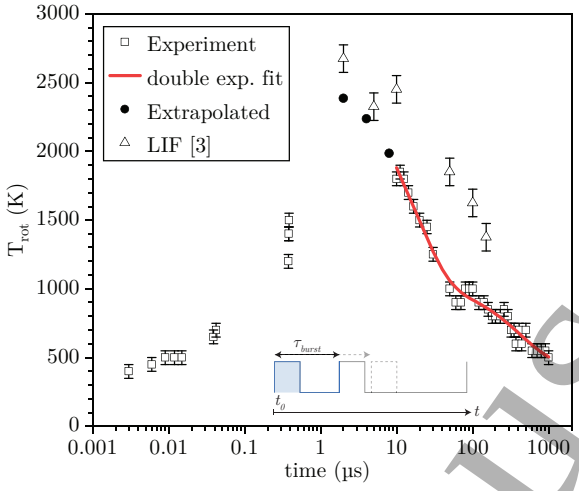

Figure 10. Gas temperature evolution in a *Type I* pulse and its after-pulse, with double exponential fit of the temperature decay. The two decay time constants are 17 µs and 500 µs. The LIF (Laser Induced Fluorescence) data are those reported in [3].

transitions of the OH(A-X) system, $(A, v' = 1, J' = 4.5) - (X, v'' = 0, J'' = 3.5)$ and $(A, v' = 1, J' = 9.5) - (X, v'' = 0, J'' = 8.5)$. The population ratio of J'' levels is proportional to the ratio of LIF fluorescence lines, provided the collisional quenching of the upper level is constant. The collision quenching of the upper state depends strongly on J' [23]. Suppose rotational collisions (RET) quickly redistribute the excess population to the whole rotational manifold till a thermal distribution is reached. In that case, the collisional quenching in the upper state is constant, i.e. does not depend on the level J' promoted by laser absorption. The measurement of [3] were analysed under this hypothesis. Recent investigation reveals that rotational thermalisation in our conditions does not occur and, on the contrary, most of the fluorescence comes from the laser-excited J' level [7, 8]. A correction factor equal to the ratio of the quenching rate coefficient of $J' = 4.5$ and $J' = 9.5$ should be used for the ratio of the lines. This specific ratio is not available in [23], and, in addition, it can change in time due to the change in the mixture composition. However, a quenching ratio of about 0.5 forces the LIF temperatures to match the SPS values. This value is in line with the J' dependence reported in [23]. We then conclude that this is the reason for the discrepancy between LIF and SPS temperatures and that

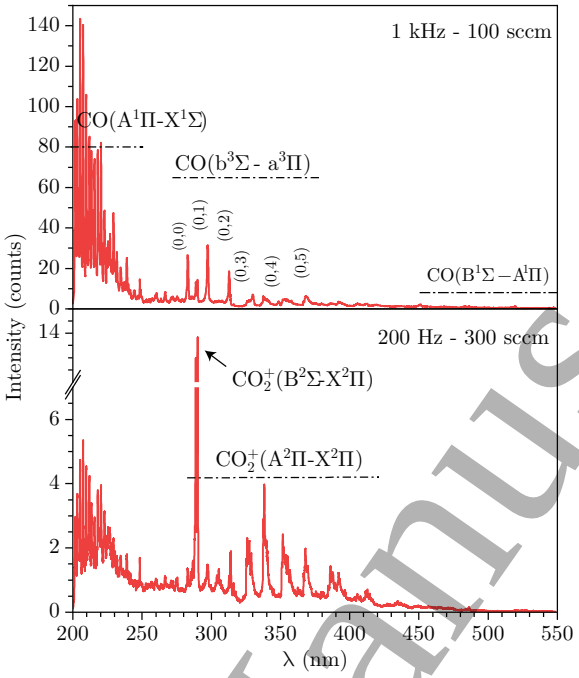

Figure 11. Comparison between emission spectra observed in Region I under different operating conditions in pure CO_2 gas.

the latter are more reliable.

4.4. Spectra in Type I pulses

Here and in the following section 4.5 we shall discuss spectra below 550 nm, since the region at higher wavelengths does not show interesting features except for two oxygen lines.

4.4.1. Region I Spectra at the beginning of a discharge event are shown in figure 11. Two continuous mode (CW) conditions are compared: (a) 1 kHz and 100 sccm and (b) 200 Hz and 300 sccm. Since the temporal evolution of the total discharge light in Region I strictly follows the current pulse, electron impact excitation is the dominant precursor of the emission. Five band systems are observed in the 190–550 nm range (see [24, 25] for CO bands, [26, 27] for $CO_2{}^+$ bands):

i) the CO *Fourth Positive System* - 4^{th}PS, $A^1\Pi - X^1\Sigma$ in the 200–250 nm range;

ii) the CO *Third Positive System* - 3^{rd}PS, $b^3\Sigma - a^3\Pi$ in the 285–350 nm range;

iii) weak bands of the CO *Angstrom System* $B^1\Sigma - A^1\Pi$ in the 450–550 nm range

iv) the $CO_2{}^+$ *Fox Duffendack Barker System* - FDBS, $A^2\Pi - X^2\Pi$ in the range 280–450 nm;

v) the $CO_2{}^+$ $\lambda\lambda 2883 - 2896$ System $B^2\Sigma - X^2\Pi$.

According to [24], these latter two bands are favored by relatively energetic excitation, like in negative glows, hollow cathode and electron beams.

In the 1 kHz condition (a), all these systems are observed, while the two CO systems drop dramatically at 200 Hz and higher gas flux (b). As shown in [3], the final CO_2 dissociation after few pulses amounts to about 20 %. At 1 kHz, the gas in the discharge gap is not yet entirely renewed, and each discharge pulse occurs in a gas mixture containing still some CO. In condition (b), the gas refreshing between two pulses is almost complete, such that only trace amounts of CO and O_2 are expected. A very low level of CO emissions is detected in condition (b), leading to thinking that the degree of CO_2 dissociation in Region I is small.

Due to the disappearance of the 3^{rd}PS of CO, the $CO_2{}^+$ systems emerge. To our knowledge, besides photographic plates, a plot of the FDBS bands has been published only in [17], in the 300–390 nm range, in which some superposition of the

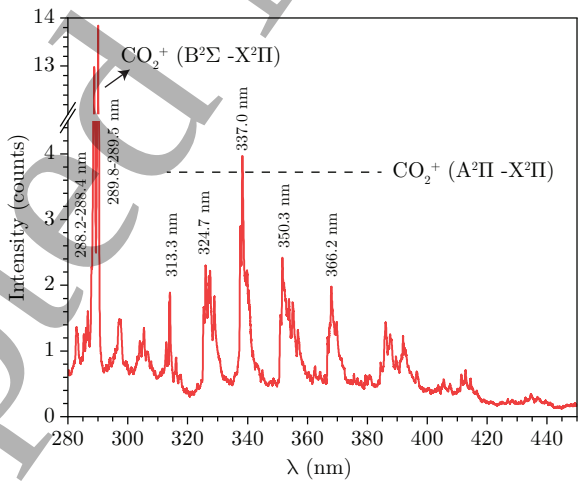

Figure 12. Detail of the $CO_2{}^+$ bands. Bandheads wavelength from [24]. For a more detailed overview of the system's transition wavelengths refer to [26] and [27].

CO 3^{rd}PS is still present and the $CO_2{}^+$ $\lambda\lambda 2883-2896$ System is excluded. Since it might be of some interest, we show in more detail our measurement of the $CO_2{}^+$ systems in figure 12.

4.4.2. Regions II and III These two regions present similar spectroscopic features, such as those reported in figure 5(b). Here we find the characteristics of a spark regime, with a relatively low voltage and a very high electron density in the range 10^{17}–$10^{18}\,\mathrm{cm}^{-3}$. CO and $CO_2{}^+$ emissions disappear. This must be ascribed to a lower electron energy, compared to that in Region I, unless we assume that CO_2 is already totally dissociated. Neutral and ionized atomic lines (C, C^+, C^{++} and O) appear along with seemingly two continua (200–350 nm and 350–450 nm), with unidentified bands superimposed to them. This might appear in contradiction with the lower electron energy invoked to explain the disappearance of electron impact molecular bands. Atomic lines are much more intense than molecular bands at high pressure since they have higher Einstein coefficients. CO 4^{th}PS and 3^{rd}PS bands have Einstein coefficients of the order of $10^7\,\mathrm{s}^{-1}$ or less [25], which must be compared with the $1.37\cdot 10^8\,\mathrm{s}^{-1}$ and $5.61\cdot 10^7\,\mathrm{s}^{-1}$ values for C^{++}(229.68 nm), C^+ (251.2 nm) respectively (see NIST atomic spectra database [22]). In the collision-dominated conditions of our system, in which the electronic quenching is much faster than the radiative decay, this results in a quantum yield for the ionic lines that is one order of magnitude larger than the one for molecular bands.

The continuum emission is perhaps due to a combination of processes. The $CO + O \rightarrow CO_2 + h\nu$ recombination chemi-luminescence continuum [17, 28, 29] must be ruled out, since it does not correspond to our observations. The continuum emission might be ascribed to electron-ion recombination and to electron-neutral/ion Bremsstrahlung. For the former, we have no clues about possible spectra. Electron-neutral Bremsstrahlung continuum has been reported many times in atmospheric pressure discharges [30–36]. In some cases, it has even been used for electron density and temperature measurements [31, 32, 35, 36]. Looking at the Bremsstrahlung spectra shown in [30, 36] calculated at various electron temperatures, we find that they are not conflicting with our spectra if we assume an electron temperature in the range 1-2 eV. Also, when the electron density is higher, a contribution from electron-ion Bremsstrahlung can be present. The bands in the 350–450 nm spectral range are unidentified. They might belong to the CO flame bands system [29, 37], due to the recombination $CO + O + M \rightarrow CO_2{}^* + M$ followed by light emission from

the CO_2 excited state. However, the bands of the CO flame system reported in [24] do not correspond to those observed here (figure 5). Another argument rules out any CO+O origin of these emissions: both continua and bands do not survive after roughly Region III. On the contrary, CO+O recombination should still be active for many tens of µs after the discharge pulse [3]. Any other known band of neutral or singly ionized CO_2, O_2 or CO does not correspond to these bands. We believe that the origin of this light should be looked for in ion-electron recombination processes, although we have found no mention in the literature.
Finally, in Region IV, we just find neutral atomic lines and a well defined C_2 Swan system. In this temporal region, the current is low, and the electron energy should also be so low as to exclude any electron impact excitation.

4.5. Spectra in Type II pulses

We have measured spectra of *Type II* pulses in the second pulse of a two-pulse burst, in which the second pulse is triggered with a delay of 11 µs after the first one. Three such spectra are shown in figure 13. At the beginning of the pulse, the spectrum shows a strong C(247 nm) line and the bands of the $CO_2{}^+$ FDBS System. CO 4^{th} and 3^{rd} PS bands are weak or absent, as well as the $\lambda\lambda 2883 - 2896$ System. To better appreciate these statements, the spectrum of figure 11(b) is also plotted in figure 13(a). Comparing these two spectra must consider that the gas and rotational temperatures at the beginning of the second pulse are high, around 1800 K (section 4.3), contrary to roughly 400 K at the start of the first pulse. The absence of CO emissions contrasts with the large amounts of CO generated by the first pulse (as measured in the effluent gas, i.e. in the late post-pulse [3]) and with the presence of $CO_2{}^+$ bands. One possibility is that CO is totally dissociated immediately after the first pulse and that it is formed later by recombination. It seems highly unlikely that after 11 µs no recombination has yet occurred. The other possibility is that in *Type II* pulses, the initial electron temperature is much lower than in Region I of *Type I* pulses, and the $CO_2{}^+$ FDBS System emission is not due to direct electron impact from the CO_2 ground state. Another process might be operative, probably involving directly the $CO_2{}^+$ ions. The process must be different because contrary to the Type I Region I spectra, here the $CO_2{}^+$ $\lambda\lambda 2883 - 2896$ System is not seen.
Moving on in time, spectra soon change drastically towards those shown in figure 13(b)(c). New spectral features that have not been observed in any Region

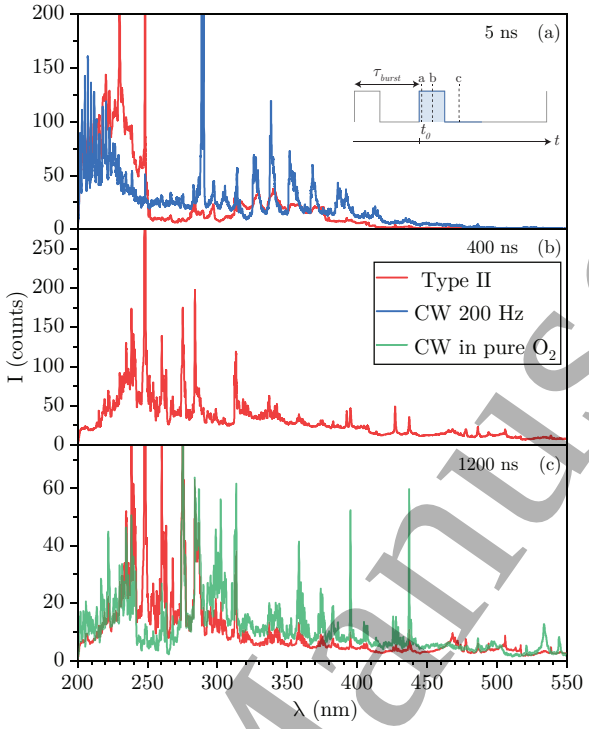

Figure 13. Spectra measured in a *Type II* pulse at three delays from the voltage start. Second pulse of a 2-pulse burst fired at 11 µs after the first pulse. In (a), the spectrum of figure 11(b) is plotted for comparison. In (c), the spectrum obtained in a continuous 200 Hz discharge in pure O_2 is also plotted for comparison.

of *Type I* pulses appear. Again, we have not been able to assign these bands to any known ones of neutral or singly ionised CO_2, O_2 or CO. We can observe similar emissions when running the discharge with a pure O_2 gas feed. The comparison of spectra plotted in figure 13(c) shows a clear correspondence of these bands systems, apart from the absence of C atomic lines and C_2 Swan bands in pure oxygen and intensity mismatches easily ascribable to the different discharge conditions. We conclude that these emissions are the spectral signature of the massive presence of O_2 in the initial gas composition of this *Type II* discharge pulse. Note that these O_2-related bands are not observed in Region I, II and III of *Type I* pulses. They start to appear, very weakly, at the end of Region III. This suggests that O_2 formation in the first pulse is not significant in Regions I and II, but starts in Region III and develops in Region IV.

5. Summary

The time-resolved spectroscopy permits an overall description of the discharge characteristics, quantitative in some cases, qualitative in others. *Type I* pulses, i.e. the initial pulse of a burst, or all the pulses in CW operation with repetition rates not exceeding roughly 10 kHz, have a definite temporal structure with essentially two phases:

i) a breakdown phase, Region I, dominated by electron impact processes. The electron energy distribution function (EEDF) cannot be estimated by spectroscopic means. All the emission bands are certainly related to electron-molecule excitation, and the electron density is not determined due to the lack of spectral resolution of our detection system. The EEDF is likely non-Boltzmann, with a relatively large amount of high energy electrons, while the overall electron density should be not very high, certainly less than $10^{17}\,\mathrm{cm}^{-3}$. The gas temperature remains close to ambient values. No spectroscopic markers, namely CO bands emission, of a significant CO_2 dissociation are present.

ii) a spark regime, likely characterised by a two-temperatures LTE, with electron temperature of approximately 2-2.6 eV, electron density in the range 10^{17}–$10^{18}\,\mathrm{cm}^{-3}$, gas temperature slightly above 2000 K. The ionisation degree is quite high, with a maximum value of around 5 %, but far from the full ionisation found in [11]. The two-temperature LTE is then justified by the inefficient electron-neutral thermal contact (see, for ex. [38]) and by the ionisation degree. The spark regime emission is dominated by atomic lines and (except for the C_2 Swan bands) by unknown bands and continua perhaps related to ion recombination processes. No distinguishable electron impact emissions are observed, likely due to a drop of electron energy relative to the breakdown phase and the appearance of superimposed stronger emissions. We cannot then ascribe the absence of CO bands to a still low level of CO_2 dissociation. CO bands are in fact not seen at the beginning of *Type II* pulses, where the amount of CO should be significant.

Type II pulses show a sudden transition to the spark phase, such that electron impact emissions can eventually be observed in the first 10 ns of the discharge. Most energy is dissipated in a spark regime, contrary to the *Type I* case in which the most significant part of electrical energy is spent in the breakdown phase. Electron temperature and density are similar to the previous case. The initial gas composition

is, instead, different. Clear spectroscopic markers show the abundant presence of O_2 in the initial gas mixture.

From the point of view of chemical reactions, we point out the following considerations. The combined spectroscopic observations of both pulse types lead us to conclude that CO_2 dissociation and O_2 formation is an ongoing process along and after Region III of the first pulse. The O_2-related bands observed from the beginning of *Type II pulses* are not observed in Region II, and in Region III they appear at late times with low intensity. Therefore, the largest amount of CO_2 dissociation, followed by O_2 formation, seems not to happen in the first part of the pulse, where the electron energy is higher, but later and perhaps even after the discharge current has dropped. A long-lasting mechanism, possibly related to the vibrational excitation of CO_2, is then active. The high electron density and the electron temperature value of about 2 eV fit the conditions for the highest rate coefficients of CO_2 vibrational excitation, as calculated in [39]. Therefore, the spark regime has the proper conditions for an enhanced role of the vibrational mechanism of CO_2 splitting, which might explain the better performance of the burst mode compared to the CW mode, in terms of higher dissociation degree and energy efficiency [5]. These observations agree with the results of model calculations reported in [4], where electron impact with vibrationally excited CO_2 was shown to be the most important dissociation channel in a NRP discharge. Of course we cannot exclude a role for thermal dissociation, and CO_2^+ dissociative recombination [40], which might come into play thanks to the high gas temperature and ionisation degree. These channels were anyway accounted for and found to be minor in [4], where a peak electron density of about $5{\cdot}10^{17}\,\mathrm{cm}^{-3}$ was calculated (see the supplemental information of the paper).

A comparison of the present measurements with literature data is not straightforward. Spectroscopic observations in CO_2 discharges have been reported in different devices at atmospheric pressure, like microwave discharges or dielectric barrier discharges, with totally different plasma conditions and without any time resolution. Instead, similar studies on NRP discharges, have been conducted in N_2 only, as mentioned in the introduction. With the due distinctions relevant also to the many differences in electrodes shape and gap, together with power supply units and applied voltage, we basically find similar plasma conditions. A transition from streamer to spark and a spark phase characterised by moderate electron temperature and high ionization degree, although we do not reach the almost full ionization found in [11]. Furthermore, our spark phase is characterised by a two-temperature LTE

similar to that in [38], and different from the single-temperature LTE assumed in [11]. Nevertheless, we cannot exclude that such extreme conditions can be also reached in CO_2, with proper electrodes shape and gap, and applied voltage. Unfortunately, literature data cannot help us identify the unknown bands and continua observed in the spark regime, mainly in the 300–500 nm range. We speculate as being due to ion recombination processes and Bremsstrahlung.

6. Conclusions

The NRP discharge in CO_2 has proven to be a challenging plasma environment for emission spectroscopy investigations. Not all the emission features have been identified, and those bands that could be useful as diagnostic tools are not readily available. Nevertheless, plasma parameters can still be inferred, thanks to the presence of atomic neutral and ionic lines, and the existence of LTE (EEK) conditions. Partial spectroscopic thermometry is feasible, although misinterpretations of C_2 and CN emissions must be avoided (see Appendix B). Some purely qualitative guesses can be made on the evolution of the gas mixture, although they need support from kinetic modeling and more direct measurements, like CET-LIF [3, 8]. As a whole, the sum of all the spectroscopic observation and analysis returns the coherent picture of a discharge evolving from a breakdown phase towards a spark phase, the latter presenting favourable conditions for robust vibrational pumping that might promote an efficient CO_2 dissociation by vibrationally enhanced mechanisms.

Further progress can also be achieved by implementing more controllable discharge conditions, avoiding voltage reflections and re-triggering by a 75 Ω dummy matched load grounding of the cathode. This would provide a clear-cut separation of Region I from the spark regime to help solve whether CO_2 is mainly dissociated in the latter. Finally, it is worth pointing out that the plasma conditions we have explored are quite a new realm for plasma chemistry. In particular, we refer to the very high ionisation degree, which might open unexplored ion chemistry. For example, charge exchange reactions might affect the vibrational kinetics, like those reported for hydrogen: $H_2^+ + H_2 \rightarrow H_2(v) + H_2^+$, [41]. Or, in addition to V-V pumping, the vibrational ladder might be climbed by $CO_2(v) + e \rightarrow CO_2(v + \Delta v) + e$, [42], thanks to a large number of low energy electrons.

Acknowledgements

This project has received funding from the European Union's Horizon 2020 research and innovation programme under the Marie Skłodowska-Curie grant agreement No. 813393. M. Ceppelli acknowledges support by the Progetto Strategico di Ateneo ERICSOL of the University of Trento.

Appendix A. Stark Broadening

The Stark broadening parameters of oxygen and carbon lines used for electron density measurements are reported in table A1. The broadening of the carbon line is almost one order of magnitude smaller than that of the oxygen line. Therefore, we use the more sensitive oxygen line for the whole range of measurements, and the carbon line broadening is used for comparison in the conditions of maximum electron density only. The other broadening processes outside of instrumental and Stark broadening – i.e. natural, resonant, Doppler and Van der Waals broadening – are of such size that they can be considered negligible (see table A2). Therefore, an isolated line shape is the result of a convolution between the instrumental function and the Stark broadening.

For the atomic oxygen multiplet the relative line strengths of the constituents are treated as fit parameters. In fact outside of the different fine structure components (relative ratios: 1:0.73:0.43 in order of decreasing photon energy [47]), there are, in addition to electron impact, other effects that cause different population of the upper excited state sublevels [48] – i.e. population of the $3p\ ^5P^J$ states by the $5s\ ^5S$ level with different Einstein coefficient per transition. This weighting is mainly relevant to reproduce the measured asymmetric line shape of the triplet in conditions where there is little additional broadening outside of instrumental broadening (see figure A1).

The instrumental function for the system is determined to be a Voigt profile from a fit of the oxygen triplet in the Stark free afterglow (4.5 µs after discharge) of an O_2 discharge. In our setup the Voigt profile is the convolution of a Gaussian, standard deviation $\sigma = (85.7 \pm 0.5)$ pm, with a Lorentzian, HWHM $\gamma = (71.4 \pm 0.6)$ pm. The resulting broadening FHWM is (0.29 ± 0.01) nm (table A2). This approach was chosen over the measurement of the line shape of a narrow bandwidth light source, like a diode laser. The latter would fail to capture additional instrumental broadening caused by the fact that each subsequent burst channel is spatially uncorrelated and

Table A1. Stark broadening parameters for the investigated oxygen and carbon transitions. Theoretical values for (i) oxygen, based on data from NIST and TOPbase and accounting for LS-coupling, and (ii) carbon, calculated by Griem [43], evaluated at constant $n_e = 10^{16}\,\mathrm{cm}^{-3}$. In addition the experimentally measured total (electron+ion) Stark width parameter for carbon at $n_e = 1.08 \cdot 10^{17}\,\mathrm{cm}^{-3}$ from [44] is also shown. Here w_e is the electron impact width in Å and α the ion impact parameter in Å.

Transition	**Source**	T_e(K)	w_e (Å)	α (Å)
O $3s\ ^5S_0 \leftarrow 3p\ ^5P^J$	NIST-LSJ [45]	5000	$4.74 \cdot 10^{-2}$	$2.45 \cdot 10^{-2}$
		10000	$5.38 \cdot 10^{-2}$	$2.46 \cdot 10^{-2}$
		20000	$7.10 \cdot 10^{-2}$	$2.47 \cdot 10^{-2}$
		40000	$9.88 \cdot 10^{-2}$	$2.48 \cdot 10^{-2}$
O $3s\ ^5S_0 \leftarrow 3p\ ^5P^J$	TOPbase [45]	5000	$5.52 \cdot 10^{-2}$	$3.13 \cdot 10^{-2}$
		10000	$6.30 \cdot 10^{-2}$	$3.14 \cdot 10^{-2}$
		20000	$8.25 \cdot 10^{-2}$	$3.15 \cdot 10^{-2}$
		40000	$1.13 \cdot 10^{-1}$	$3.16 \cdot 10^{-2}$
C $2p\ ^1S \leftarrow\ 3s\ ^1P$	Griem [43]	5000	$6.34 \cdot 10^{-3}$	$2.7 \cdot 10^{-2}$
		10000	$7.22 \cdot 10^{-3}$	$5.3 \cdot 10^{-2}$
		20000	$8.34 \cdot 10^{-3}$	$1.1 \cdot 10^{-1}$
		40000	$9.40 \cdot 10^{-3}$	$2.1 \cdot 10^{-1}$
	Experimental [44]	17600	$7.40 \cdot 10^{-3}$	-

therefore imaged differently by the collection system.

Examples of fitted line shapes are shown in figure A1. In the instance of a narrow line that does not resemble the instrumental triplet line shape (dash-dotted line), it has to be discarded manually as it results from noise or poor signal-to-noise ratio.

The electron density n_e is obtained from the fitted Stark broadening by the following formula [49]:

$$\Delta\lambda_{Stark} = 2 \cdot w_e \cdot n_e \cdot 10^{-16} \cdot \big(1 + 1.75 \cdot 10^{-4} \cdot n_e^{1/4} \cdot \alpha \cdot (1 - 0.068 \cdot n_e^{1/6} \cdot T_g^{-1/2})\big)\,, \tag{A.1}$$

where $\Delta\lambda_{Stark}$ is the Stark broadening FWHM (in Å), n_e the electron density (in cm^{-3}), T_g the gas temperature (in K), w_e and α respectively the electron and

Table A2. Full width half maximum for different broadening mechanisms calculated using theory from [46] with values of parameters used in the calculation. Values picked to resemble operating conditions of the discharge, whilst maximising the estimated broadening. For Doppler broadening T_g is the gas temperature at peak value [4] in a similar discharge, for resonant broadening $n_a(g)$ is the oxygen ground state density assumed to be ideal gas number density at 300 K, and for Van der Waals broadening gas temperature T_g and pressure p are respectively ambient temperature and pressure. Measured instrumental broadening and estimated limits of Stark broadening are shown as well.

Broadening	**FWHM** est. (nm)	**Parameters**
Natural	$\leq 1 \cdot 10^{-5}$	
Doppler	$\leq 2 \cdot 10^{-2}$	$T_g = 3500\,\mathrm{K}$
Resonant	$\leq 1 \cdot 10^{-3}$	$n_a(g) = 2.7 \cdot 10^{19}\,\mathrm{cm}^{-3}$
Van der Waals	$\leq 2 \cdot 10^{-2}$	$T_g = 300\,\mathrm{K}$, $p = 1.0\,\mathrm{atm}$
Instrumental	0.29 ± 0.01	
Stark (max.)	$\lesssim 2.1$	$n_e = 2 \cdot 10^{18}\,\mathrm{cm}^{-3}$, $T_e = 5000\,\mathrm{K}$
Stark (min.)	$\gtrsim 2.3 \cdot 10^{-2}$	$n_e = 10^{16}\,\mathrm{cm}^{-3}$, $T_e = 40000\,\mathrm{K}$

ion impact parameters (in Å) that are transition specific and electron temperature (T_e) dependent, see table A1. The electron temperature is estimated in section 4.2. For the gas temperature in equation A.1, we have used the measurements reported in figure 10. In the *Type II* pulse we assumed that T_g behaves similarly to the first pulse but starting from an initial temperature of 1800 K up to 4200 K at 2.0 µs. Due to how eq. A.1 scales with temperature, the effect is mainly important in the first pulse. Calculated n_e for the discharge running at 200 Hz in 90.0 kHz burst mode for different input energies are shown in figure 7.

As cross-check on the validity of the method, the Stark broadening of the C $2p\,^1S \leftarrow 3s\,^1P$ transition (table A1) has been measured as well. It has an order of magnitude lower Stark broadening, providing a worse dynamic range in comparison to atomic oxygen. In figure A2, a comparison between observed broadening and calculated densities is shown for the oxygen and carbon transitions during the first 100 ns in the second pulse, where $\Delta\lambda_{Stark}$ is largest and appreciable for carbon. Results are consistent in the order of magnitude, despite the large difference in Stark width and usage of different sets of broadening parameters. Therefore, the obtained

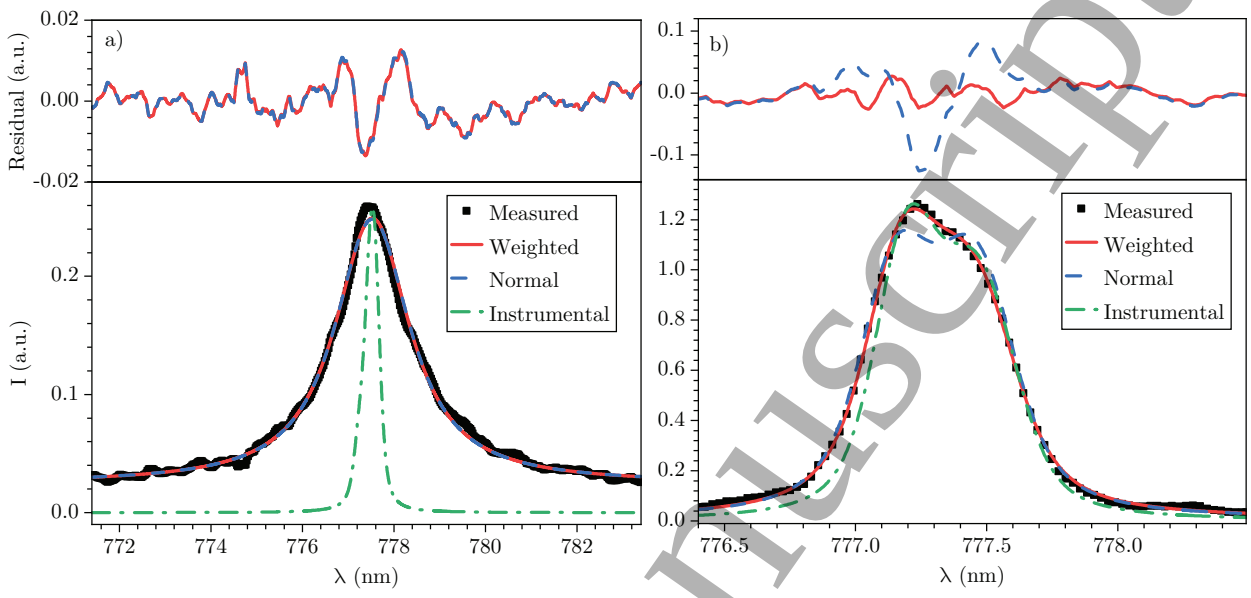

Figure A1. Comparison of fitting Lorentzian broadening with a weighted and unweighted (normal, i.e. fixed fine structure components) oxygen triplet in two regimes: low emission but strong broadening (left, 105 ns in discharge pulse) and medium emission with weak broadening (right, 945 ns in discharge pulse). The convolution of the instrumental function with the fitted relative line strength of the oxygen triplet is shown to illustrate the process. At medium to strong broadening the individual line weighting is less relevant to the overall agreement of the fit, but at weak broadening it is crucial.

densities seem reliable within 60 % taking into account the accuracy of the broadening parameters as well as the fact that T_e is not accurately known.

Appendix B. Gas Temperature

The spectroscopic measurement of the gas temperature assumes that the rotational temperature of the vibro-electronic state which emits radiation is in equilibrium with, or reproduces, the gas kinetic temperature. Translational-rotational equilibrium is achieved if the frequency of collisional rotational energy transfers (RET) is much larger than the total quenching rate (radiative + collisional) of the vibro-electronic state. In gas mixtures with molecular gases, like in the present case, this is not guaranteed. The case of the OH 3064 Å system is a striking example, as reported

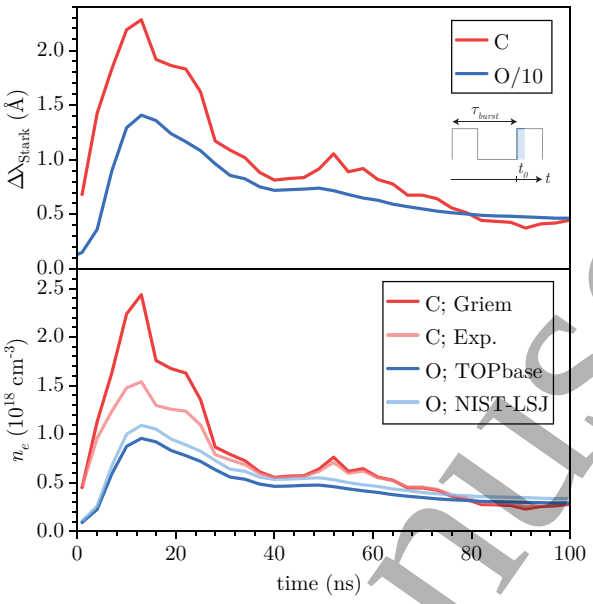

Figure A2. Comparison between Stark width (a) and electron density (b) obtained from O $3s\ ^5S_0 \leftarrow 3p\ ^5P^{J=1,2,3}$ (reds) and C $2p\ ^1S \leftarrow 3s\ ^1P$ (blues) in second pulse of discharge operating under same conditions as the 72 % setting in figure 7. Oxygen Stark width is divided by a factor of 10. Electron densities calculated from data from table A1 and for $T_e = 20\,000$ K where applicable.

in [8]. Some emissions in this paper, and generally in atmospheric pressure discharges, arise from vibro-electronic states resulting from energy transfers or recombinations or chemi-luminescent reactions, in which part of excess energy flows into rotational excitation. The result is a highly non-equilibrium nascent rotational distribution that cannot be representative of the gas temperature if not allowed to reach equilibrium. We shall show later in this paragraph the examples of the CN Violet system and the C_2 Swan bands. In diatomic molecules, in particular homonuclear ones, electron impact excitation of vibro-electronic states reproduces the rotational excitation of the ground state onto the excited states. In this case, even if RET collisions are not sufficient to reach equilibrium, the rotational temperature of the emission bands is a safe representation of the gas temperature, taken for granted that the rotational and translational degrees of freedom are in equilibrium in the ground state (see [50] for a comprehensive review of this topic). The $N_2(C^3\Pi_u - B^3\Pi_g)$ SPS emission fulfills these requirements, provided it is due to electron impact only.

SPS can be observed and used to determine the gas temperature if a small percentage of N_2 is injected in the gas feed. The hypothesis of pure electron impact excitation might be invalidated by coming into play of the Pooling reaction $N_2(A) + N_2(A) \longrightarrow N_2(C) + N_2(X)$, giving rise to a different nascent rotational distribution in $N_2(C)$. A couple of considerations rule it out. First, the measurement is limited to the very first nanoseconds of the discharge. The metastable states' concentration grows more slowly. Their quenching is faster than the time between the discharge regions, such as to exclude a built-up of their concentration between discharge regions. Second, the vibrational distribution of $N_2(C, v)$ by Pooling reactions features a characteristic population inversion between $v = 1$ and $v = 0$ [51, 52], that is not observed in the SPS spectra, as far as they are observable, i.e., again, at the very beginning of the discharge regions. Instead, the $N_2(C, v)$ distribution is still electron impact-like. We have chosen the (0,0) band at 337 nm, which is the strongest and less overlapped by other emissions.

Bands of the CN ($B^2\Sigma^+ - X^2\Sigma^+$) are also readily seen when nitrogen is added to the mixture, starting few nanoseconds after the discharge ignition, in Region I, and remaining visible when there is no discharge current. It is clear that they do not originate from electron impact excitation, but likely from the recombination $C + N + M \rightarrow CN(A, B) + M$, which is known to generate supra-thermal vibrational and rotational population distribution functions (see [53] and references therein).

In figure B1, the spectrum of the $\Delta v = 0$ bands sequence of the CN violet system is shown, together with N_2 SPS bands, measured at 9 ns in Region I. Rough simulation of the spectrum shows that a high rotational temperature, about 2500 K, is required, as contrasted to the 400-500 K temperature recovered from the SPS bands. We deduce that RET collisions are insufficient to equilibrate the CN(B) rotational excitation within its lifetime.

C_2 ($d^3\Pi_g - a^3\Pi_u$) Swan bands show the same problem. These bands start to be observed clearly against other overlapping emissions in the tail end of Region III of the first and second pulse. In figure B2, we report the cleanest Swan bands spectrum we have measured, at 2 µs in the 1 kHz, CW case. The simulated spectra show that a rotational temperature of about 6000 K is observed, while lower temperatures are far from providing a good match with the measured spectrum. Such a high temperature is unreasonably higher than those obtained by SPS fitting. The Swan bands are generated by the recombination $C(^3P) + C(^3P) + M \rightarrow C_2(d^3\Pi_g) + M$ ([18] and references therein) with excess energy resulting then in a high nascent

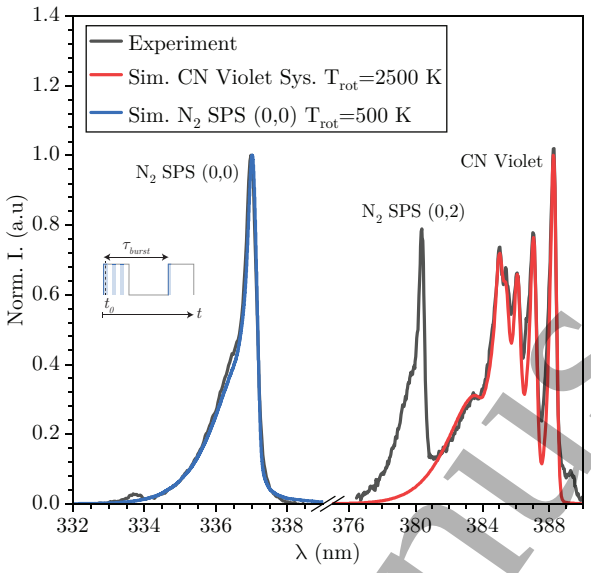

Figure B1. Spectrum recorded at 9 ns in the first pulse, with N_2 SPS bands and the $\Delta v = 0$ sequence of the CN Violet System. The SPS (0,0) band is simulated with the DIATOMIC software [54] and the spectroscopic constants of [55]. The CN emission is simulated by LIFBASE [56].

rotational energy that is not forced to equilibrium by RET collisions, due to an electronic quenching faster than RET. The Swan system must then be discarded as a temperature monitor.

References

[1] Scapinello M, Martini L M, Dilecce G and Tosi P 2016 *J. Phys. D: Appl. Phys.* **49** 075602
[2] Montesano C, Faedda M, Martini L M, Dilecce G and Tosi P 2021 *Journal of CO2 Utilization* **49** 101556 ISSN 2212-9820
[3] Martini L M, Lovascio S, Dilecce G and Tosi P 2018 *Plasma Chem Plasma Process* **38** 707–718
[4] Heijkers S, Martini L M, Dilecce G, Tosi P and Bogaerts A 2019 *J. Phys. Chem. C* **123** 12104 – 12116
[5] Montesano C, Quercetti S, Martini L M, Dilecce G and Tosi P 2020 *Journal of CO_2 Utilization* **39** 101157
[6] Martini L M, Gatti N, Dilecce G, Scotoni M and Tosi P 2018 *Plasma Phys. Controlled Fusion* **60** 014016 ISSN 1361-6587
[7] Dilecce G, Martini L, Ceppelli M, Scotoni M and Tosi P 2019 *Plasma Sources Sci. Technol.* **28** 025012

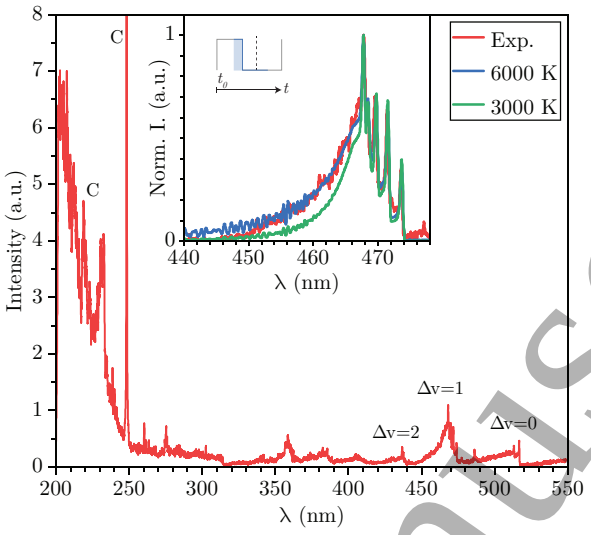

Figure B2. Spectrum recorded at 2 µs in the CW, 1 kHz condition, showing clear sequences of the C_2 Swan bands. Only three sequences are labelled. In the inset figure, the $\Delta v = 1$ sequence is compared with simulated spectra at 6000 K and 3000 K. The simulations are made by DIATOMIC software [54], using the constants suggested in [25].

[8] Ceppelli M, Martini L M, Dilecce G, Scotoni M and Tosi P 2020 *Plasma Sources Sci. Technol.* **29** 065019

[9] Lo A, Cessou A, Lacour C, Lecordier B, Boubert P, Xu D A, Laux C O and Vervisch P 2017 *Plasma Sources Sci. Technol.* **26** 045012

[10] Orrière T, Moreau E and Pai D Z 2018 *J. Phys. D Appl. Phys.* **51** 494002

[11] Minesi N, Stepanyan S, Mariotto P, Stancu G D and Laux C O 2020 *Plasma Sources Sci. Technol.* **29** 085003

[12] Shcherbanev S A, Khomenko A Y, Stepanyan S A, Popov N A and Starikovskaia S M 2017 *Plasma Sources Sci. Technol.* **26** 02LT01

[13] Shcherbanev S A, Ding C, Starikovskaia S M and Popov N A 2019 *Plasma Sources Sci. Technol.* **28** 065013

[14] Silva T, Britun N, Godfroid T and Snyders R 2014 *Plasma Sources Sci. Technol.* **23** 025009

[15] Silva T, Britun N, Godfroid T and Snyders R 2016 *Plasma Process Polym.* **14** e201600103

[16] Raposo G J C, van de Steeg A, Mercer E, van Deursen C, Hendrickx H, Bongers W, Rooij G J V, de Sanden R V and Peeters F 2021 *Journal of Physics D: Applied Physics*

[17] Rond C, Bultel A, Boubert P and Chéron B G 2008 *Chem. Phys.* **354** 16 – 26

[18] Carbone E, D'Isa F, Hecimovic A and Fantz U 2020 *J. Quant. Spectrosc. Radiat. Transfer* **29** 055003

[19] McWhirter R W 1965 *in: R.H. Huddlestone, S.L. Leonard (Eds.), Plasma Diagnostic*

Techniques, Academic Press, New York 201–264
[20] Cristoforetti G, De Giacomo A, Dell'Aglio M, Legnaioli S, Tognoni E, Palleschi V and Omenetto N 2010 *Spectrochimica Acta Part B: Atomic Spectroscopy* **65** 86 – 95
[21] van der Mullen J A M 1990 *Phys. Rep.* **191** 109 – 220
[22] Kramida A, Yu Ralchenko, Reader J and Team N A 2020 NIST Atomic Spectra Database (ver. 5.8), [Online]. Available: `https://physics.nist.gov/asd` [2020, December 18]. National Institute of Standards and Technology,Gaithersburg, MD. URL `https://physics.nist.gov/PhysRefData/ASD/LIBS/libs-form.html`
[23] Copeland R A, Dyer M J and Crosley D R 1985 *J. Chem. Phys.* **82** 4022–4032
[24] Pearse R W B and Gaydon A G 1976 *The identification of molecular spectra* 4th ed (John Wiley & Sons - New York)
[25] da Silva M L and Dudeck M 2006 *Journal of Quantitative Spectroscopy & Radiative Transfer* **102** 348 – 386
[26] Gauyacq D, Larcher C and Rostas J 1979 *Canadian Journal of Physics* **57** 1634–1649
[27] Johnson M A and Rostas J 1995 *Molecular Physics* **85** 839–868
[28] Broida H and Gaydon A 1953 *Trans. Faraday Soc.* **49** 1190
[29] Gaydon A G 1974 *The Spectroscopy of Flames* (Chapman and Hall, London)
[30] Park J, Henins I, Herrmann H W and Selwyn G S 2000 *Phys. Plasmas* **7** 3141–3144
[31] Iordanova E, de Vries N, Guillemier M and van der Mullen J J A M 2008 *J. Phys. D Appl. Phys.* **41** 015208
[32] Park S, Choe W, Moon S Y and Park J 2014 *Appl. Phys. Lett.* **104** 084103
[33] Bazinette R, Paillol J and Massines F 2015 *Plasma Sources Sci. Technol.* **24** 055021
[34] Pai D Z 2015 *Plasma Sources Sci. Technol.* **24** 025021
[35] Nikiforov A Y, Ionita E R, Dinescu G and Leys C 2016 *Plasma Physics and Controlled Fusion* **58** 014013
[36] Navrátil Z, Morávek T, Ráheľ J and Čech J 2017 *Plasma Sources Sci. Technol.* **26** 055025
[37] Dixon R N 1963 *Proc. Roy.Soc. A* **275** 431
[38] van der Horst R M, Verreycken T, van Veldhuizen E M and Bruggeman P J 2012 *J. Phys. D: Appl. Phys.* **45** 345201
[39] Laporta V, Tennyson J and Celiberto R 2016 *Plasma Sources Sci. Technol.* **25** 06LT02
[40] Viggiano A A, Ehlerding A, Hellberg F, Thomas R D, Zhaunerchyk V, Geppert W D, Montaigne H, Larsson M, Kaminska M and Österdahl F 2005 *J. Chem. Phys.* **122** 226101
[41] Janev R K 1987 *Elementary processes in hydrogen-helium plasmas* (Springer)
[42] Yamazaki M, Nishiyama S and Sasaki K 2020 *Plasma Sources Sci. Technol.* **29** 115016
[43] Griem H R 1974 *Spectral line broadening by plasmas* (Academic Press)
[44] Djeniže S, Srećković A and Bukvić S 01 Feb 2006 *Zeitschrift für Naturforschung A* **61** 91 – 94
[45] Alonizan N, Qindeel R, Nessib N, Sahal-Brechot S and Dimitrijevic M 2015 *Journal of Astrophysics and Astronomy* **36**
[46] Kunze H 2009 *Introduction to Plasma Spectroscopy* Springer Series on Atomic, Optical, and Plasma Physics (Springer Berlin Heidelberg)
[47] Alonizan N, Qindeel R and Ben Nessib N 2016 *International Journal of Spectroscopy* **2016** 1697561

[48] Milosavljevic V, Ellingboe A R and Daniels S 2011 *The European Physical Journal D* **64** 437–445
[49] Konjević R and Konjević N 1997 *Spectrochimica Acta Part B: Atomic Spectroscopy* **52** 2077 – 2084
[50] Bruggeman P J, Sadeghi N, Schram D C and Linss V 2014 *Plasma Sources Sci. Technol.* **23** 023001
[51] Piper L G 1988 *J. Chem. Phys.* **88** 231
[52] De Benedictis S and Dilecce G 1995 *Chem. Phys.* **192** 149–162
[53] Dilecce G, Ambrico P F, Scarduelli G, Tosi P and De Benedictis S 2009 *Plasma Sources Sci. Technol.* **18** 015010
[54] Tan X 2006 Diatomic, a spectral simulation program for diatomic molecules on windows platforms, release 1.292 Tech. rep.
[55] Gilmore F R, Laher R R and Espy P J 1992 *J. Chem. Phys. Ref. Data* **21** 1005 – 1107
[56] Luque J and Crosley D 1999 Int. rep. p99-009 Tech. rep. SRI